Special Section:
Preferential Flow

S. Garré*
J. Koestel
T. Günther
M. Javaux
J. Vanderborght
H. Vereecken

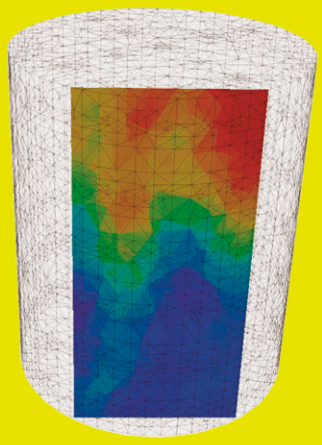

Measurements with Electrical Resistivity Tomography (ERT), TDR and effluent concentration were conducted during a step tracer experiment for two undisturbed soil columns. At the column scale the transport was essentially non-preferential in behavior, while at the scale of voxels (ERT measurements) the transport was revealed to be preferential.

S. Garré, J. Koestel, J. Vanderborght, and H. Vereecken, Agrosphere ICG-4, Forschungszentrum Jülich GmbH, Jülich, Germany; T. Günther, Leibniz Institute for Applied Geophysics, Hannover, Germany; and M. Javaux, Dep. of Environmental Sciences, UCL, Louvain-la-Neuve, Belgium. *Corresponding author (s.garre@fz-juelich.de).

Vadose Zone J. 9:336–349
doi:10.2136/vzj2009.0086
Received 27 June 2009.
Published online 3 May 2010.

Comparison of Heterogeneous Transport Processes Observed with Electrical Resistivity Tomography in Two Soils

Preferential flow in soils can manifest itself in several ways. To illustrate this, we analyzed solute transport during a step tracer experiment in two soils expected to differ in their governing transport processes: a loamy sand and a silty soil. By combining electrical resistivity tomography (ERT), time domain reflectometry, and effluent measurements, we observed different preferential flow phenomena. The transport process was characterized using voxel- and column-scale effective convective–dispersive equation (CDE) parameters, local velocities, and leaching surfaces. At the column scale, transport in the loamy sand was dominated by a homogenous convective–dispersive transport behavior, but at the scale of the voxel, preferential transport was observed. Transport in the silty soil was considerably more heterogeneous. Preferential flow was identified using ERT, voxel- and column-scale effective CDE parameters, local velocities, and leaching surfaces. In these soils, a clear influence of soil layering on solute transport was observed.

Abbreviations: BTC, breakthrough curve; CDE, convective–dispersive equation; EC, electrical conductivity; ERT, electrical resistivity tomography; LS, loamy sand; S, silt; TDR, time domain reflectometry.

Clothier et al. (2008) defined preferential flow as "all phenomena where water and solute move along certain pathways, while bypassing a fraction of the porous matrix." Based on the literature, four different preferential flow phenomena can be identified:

1. The most obvious phenomenon linked to preferential flow is, that solute concentrations in a plane perpendicular to the mean water flow direction are not homogeneous. This is often visualized with dye tracer studies (e.g., Flury et al., 1994; Flury and Wai, 2003; Burkhardt et al., 2005). The heterogeneity in solute concentrations has important consequences for reactive transport when chemical reactions depend in a nonlinear way on local concentrations (Kasteel et al., 2002; Javaux et al., 2006; Vanderborght et al., 2006). The lack of solute mixing and its effect on reactive transport is currently a major research topic in reactive groundwater transport (Cirpka et al., 2008).
2. A second way preferential flow may manifest itself is by a larger spreading of the tracer front or breakthrough curve compared with a uniform flow domain. The spreading is either defined by the second centralized spatial moment (Freyberg, 1986) of a plume or the second centralized temporal moment (Aris, 1958; Kreft and Zuber, 1978) of a breakthrough curve. Water flow in regions that bypass a part of the soil matrix leads to a rapid downward transport, whereas solutes that enter into bypassed regions move considerably more slowly. This causes an increased spreading (e.g., Adams and Gelhar, 1992; Salamon et al., 2007; Vanderborght and Vereecken, 2007).
3. A third manifestation of preferential flow is a quicker increase of the plume spreading with time or breakthrough spreading with depth than is predicted by a convective–dispersive process. In a stochastic–convective process, the spreading increases linearly with time or depth (Jury and Roth, 1990).
4. Finally, the manifestation to which preferential flow and transport are typically related is an early breakthrough with high peak concentrations and a long tailing of concentrations that decline very slowly. In this case, the breakthrough is much earlier than would be expected when flow takes place uniformly in the entire pore space or volume. Rapid leaching may result in insufficient time for chemical or biological degradation of contaminants in the root zone (e.g., Edwards et al., 1992). These contaminants then leach to the groundwater, where it may take a very long time before they are degraded (Stagnitti et al., 2003).

It must be noted that these preferential flow manifestations do not necessarily occur simultaneously. Which phenomena or characteristics are present depends on the type of preferential flow.

Several approaches have been used to quantify the different forms of appearance of preferential transport. The first type of preferential flow caused by incomplete mixing can be characterized by entropy measures such as the dilution index (Kitanidis, 1994), determination of spatial covariances of concentrations or transport parameters (Koestel et al., 2009) that characterize locally observed transport, or leaching surfaces (de Rooij and Stagnitti, 2002). The second and third types may be characterized by dispersion coefficients of laterally averaged concentrations or by spatial covariances of local advection velocities. The fourth type of manifestation may be characterized by the parameters of mobile–immobile (MIM) or dual-permeability models, which consider rapid transport in a part of the pore volume and a rate-limited solute mass exchange between different pore regions. Depending on how preferential flow manifests itself, different modeling approaches may be required to describe it. Models that may be used are the CDE model, the stream tube model, the MIM model, and the stochastic continuum model (for an overview, see Feyen et al., 1998). Using a CDE model to describe preferential flow processes may sound controversial. If preferential flow is defined more broadly than pure macropore flow with an early peak breakthrough and a long tailing, however, it may well be that a CDE model can be used to describe a transport process in which water and solutes pass a fraction of the soil matrix.

Different experimental methods and setups have been developed and used to characterize the different forms of preferential flow. Dye tracer experiments mainly focused on nonhomogeneous tracer distributions (Gjettermann et al., 1997; Burkhardt et al., 2005; Sander and Gerke, 2007). Tracer experiments in which the breakthrough is measured in the effluent of a (large) column (Schoen et al., 1999, among others) or in a field drain (Jaynes et al., 2001, among others) focus on rapid peak breakthroughs, whereas tracer experiments in which breakthrough is monitored at several depths investigate the increase of the breakthrough spreading with depth. A major problem in preferential flow and transport research is the impossibility of extrapolating one type of manifestation of preferential flow to another. For instance, spatial variations of local concentrations do not necessarily correspond with a non-Fickian dispersion process or early peak breakthrough. Neither does an early arrival of the peak concentration in combination with a long tailing of a breakthrough curve, which is observed, for instance, in columns packed with microporous glass beads (Desmedt and Wierenga, 1984), necessarily correspond to a spatial variation of macroscopically averaged concentrations. To obtain a more comprehensive insight, therefore, experimental methods that enable simultaneous observation of different manifestations of preferential flow and transport are needed. Examples of such methods are spatially discretized sampling of water and solute fluxes (Quisenberry et al., 1994; Stagnitti et al., 1999; de Rooij and Stagnitti, 2000, 2002; de Rooij et al., 2006; Bloem et al., 2009) or measuring in situ concentration breakthrough curves at several locations with suction cups or time domain reflectometry (TDR). The problem that remains with these methods is that the full three-dimensional structure of flow and transport process cannot be observed. This structure can be observed with noninvasive three-dimensional imaging techniques such as x-ray tomography (e.g., Mooney and Morris, 2008), magnetic resonance imaging at the small soil column scale (Hoffman et al., 1996; Oswald et al., 1997; Herrmann et al., 2002) or geoelectrical methods like electrical resistivity tomography (ERT) at the larger column (Binley et al., 1996; Olsen et al., 1999; Slater et al., 2002; Koestel et al., 2008) or field plot scales (al Hagrey and Michaelson, 1999; French et al., 2002; Looms et al., 2008).

The objective of this study was to characterize the different forms in which preferential transport may appear in two different soils: a loamy sand soil, which was investigated by Koestel et al. (2008), and a silty soil. Based on their textural and structural differences, solute transport was expected to be different in these two soils. We used ERT combined with TDR and effluent concentration measurements to observe solute transport and to map the spatial and temporal variation of solute (resident) concentrations. From breakthrough curves observed at different scales, the spatial variability of the transport process and scale dependence of the solute spreading were inferred using effective transport model parameters. In addition, we explored the use of leaching surfaces to characterize the underlying transport processes within the two soils.

Materials and Methods

Soils

Transport experiments were conducted on three different soil monoliths, which were sampled using large polyvinyl chloride columns with a height of 150 cm, an inner diameter of 116 cm, and a wall thickness of 2 cm. The soils were classified as a gleyic Cambisol and an orthic Luvisol (FAO, 1998). The properties of both soils are given in Table 1, and Fig. 1 shows both profiles.

One monolith was taken from an agricultural field site near Kaldenkirchen (Germany) and the soil at this site was classified as a gleyic Cambisol. The soil parent material consists of aeolian sands. At about the 33-cm depth, a sharp boundary between the plow layer and the subsoil was observed. This boundary shows an undulation oriented perpendicular to the plow direction. The bottom of the plow horizon was compacted, which indicates the presence of a plow pan. This loamy sand lysimeter will be referred to as LS.

Two monoliths were taken from intensively used arable land near Merzenhausen, where the soil was classified as an orthic Luvisol. The soil parent material at this site is loess. Earthworm burrows are abundant down to more than 150 cm, although few direct connections to the soil surface exist because of frequent plowing (Burkhardt et al., 2005). Burkhardt et al. (2005) estimated the number of earthworm burrows and root channels for four hori-

Table 1. Description of the soil horizons in both columns. Data for the Kaldenkirchen soil from Koestel et al. (2009); data for the Merzenhausen soil: textures from Burkhardt et al. (2005), saturated hydraulic conductivity (K_s) from Schmidt-Eisenlohr (2001), and bulk density (BD) and porosity from Weihermueller (2005).

Horizon	Depth	Sand	Silt	Clay	BD	K_s	Porosity
	cm	%			g cm^{-3}	$\log_{10}$(cm d^{-1})	%
Kaldenkirchen Gleyic Cambisol (loamy sand)							
Ap	0–33	72.7	22.2	5.1	1.60	0.7–2.9	40.1
Bv1	33–55	76.6	21.4	2.0	1.66	2.0–2.9	37.5
Bv2	55–70	79.1	19.7	1.2	1.60	–	40.6
Bv3	70–120	84.3	14.5	1.2	1.66	1.8–3.0	38.0
2Bv	>120	49.0	40.7	10.3	1.79	1.7–4.0	31.8
Merzenhausen Orthic Luvisol (silty soil S1 and S2)							
Ap	0–44	3	79	18	1.48	1.89	43.5
Bt	44–70	1	76	23	1.54	1.4	41.7
Bv1	70–100	1	79	20	1.54	1.4	41.7
Bv2	>100	2	84	14	1.56	1.35	40.9

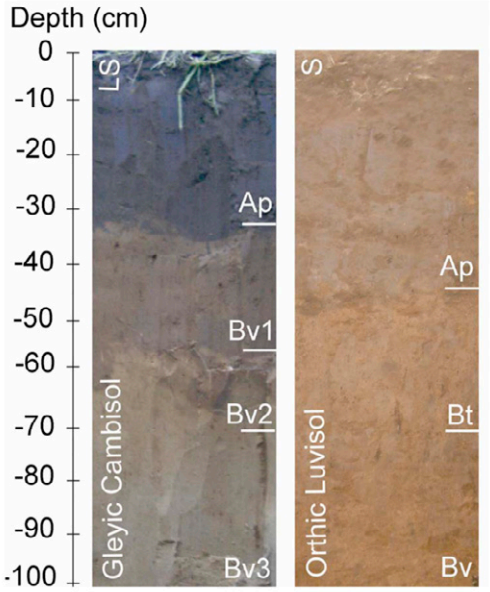

Fig. 1. Soil profiles of the loamy sand (LS) soil at the Kaldenkirchen field site (left) and the silty soil (S1/S2) at the Merzenhausen field site (right).

zontal planes in the subsoil to be about 15 and 350 × 10^{-4} cm^{-2}, respectively. These two columns will be called S1 and S2.

Lysimeter Setup

The bottom boundary of the LS lysimeter was a seepage face through which water could leave the saturated part of the flow domain. This means that there is no flux as long as the local pressure head at the bottom of the soil profile is negative. As soon as the bottom of the profile becomes saturated, a flux is assumed. This type of boundary condition very often applies to finite lysimeters that are allowed to drain under gravity. The bottoms of both the S1 and S2 lysimeters were kept at −50 kPa by a polyamid-membrane suction plate (ecoTech GmbH, Bonn, Germany) and a vacuum pump (UMS GmbH, München, Germany). The suction plate (i) avoided the formation of a saturated layer at the capillary fringe of the lysimeter, which would affect the tracer transport, and (ii) accelerated the tracer movement in the S soil, which was expected to be slower than in the LS. It was our aim to show how different transport patterns and phenomena can be distinguished and visualized using ERT rather than to compare the transport properties of the two soils under identical boundary conditions.

In all three lysimeters, 212 electrodes were inserted at the side of the column extending 1.5 cm into the soil. The electrodes were arranged in six horizontal rings of 32 equidistantly distributed electrodes. Four vertical transects of five electrodes were added between these circles (see Fig. 2). Details about the electrode arrangement were documented in Koestel et al. (2008). The electrodes were connected with relay boxes to a six-channel RESECS prototype (GeoServe, Kiel, Germany) to conduct the ERT measurements.

Horizontal TDR probes were inserted diametrically to each other in the column to measure the water content and bulk electrical conductivity. The LS lysimeter had 10 probes, whereas the S1 and S2 lysimeters had 20 each, arranged in vertical transects of five probes. We used a three-rod design (Heimovaara, 1993) with a rod length of 19 cm, a rod spacing of 2.6 cm, and a rod spacing/diameter ratio of 13:2. A TDR100 system and SDMX50 multiplexers

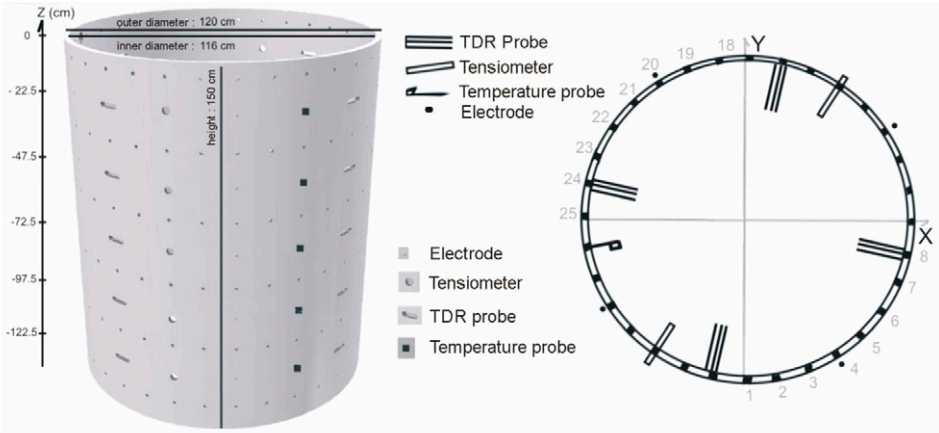

Fig. 2. Lysimeter S1/S2 with equipment (left) and horizontal cross-section of the lysimeter (right), showing locations of the time domain reflectometry (TDR) probes, tensiometers, temperature probes, and electrodes.

(Campbell Scientific, Logan, UT) were used to conduct the TDR measurements. A CR10X datalogger (Campbell Scientific) logged the data at 1-h intervals. To avoid current losses through the TDR probes, all probes were galvanically disconnected from the multiplexers during ERT measurements using relays (Koestel et al., 2008). A switchbox was used to trigger the relays automatically by using a RESECS signal.

In addition to the TDR probes, 10 tensiometers were inserted in each soil column in two diametrical transects to monitor the matric potential of the soil, as well as six platinum resistance thermometers (PT100) to be able to correct for the effect of temperature changes on the electrical resistivity. The tensiometer and PT100 sensor data were logged with a DL2e datalogger (Delta-T Devices, Cambridge, UK). The electrical conductivity of the effluent was measured with a Cond i325 conductivity meter (WTW GmbH, Weilheim, Germany). See Fig. 2 for an overview of the experimental setup.

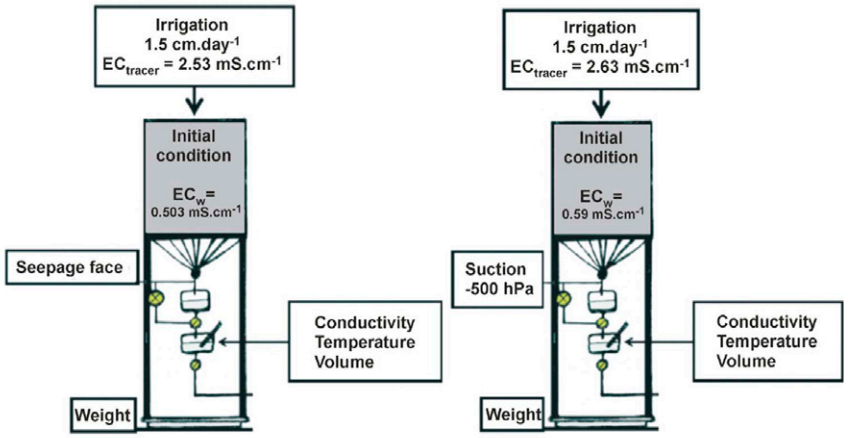

Fig. 3. Boundary conditions for the loamy sand (LS) soil (left) and the silty soil (S1 and S2) (right); EC_{tracer} = electrical conductivity of the applied tracer, EC_w = solute electrical conductivity.

Experimental Design of Tracer Experiments

The soil columns were placed in the lysimeter facility of the Forschungszentrum Jülich and were kept at a temperature of 10°C (±4°C). Steady-state flow conditions were imposed with tap water on all soil columns using a constant irrigation of 1.5 cm d^{-1} (see Fig. 3). These flow conditions were necessary to enable quantitative interpretation of the ERT images. The irrigation rate is a compromise between feasibility (due to technical [homogeneous irrigation] and temporal constraints [fast tracer displacement]) and an approximately natural boundary condition. Vanderborght et al. (2000a,b) showed that experiments run under high steady flow rates, but under a flow rate that is still relevant for rainfall rates, are still relevant for transport processes under transient boundary conditions.

The LS lysimeter was irrigated with a reservoir with 484 dripper needles. The S lysimeters were equipped with a drip tape configuration (T-Tape, John Deere Water, Moline, IL) containing 16 individual drippers. The irrigation water was at the ambient temperature of the lysimeter basement. The soil columns were at steady-state when the experiments started, with a volumetric water content varying with depth between 0.19 and 0.29 for the LS and between 0.30 and 0.43 for the S (see Table 2). After steady-state conditions were obtained for water flow as well as solute concentration, a $CaCl_2$ tracer was applied until the tracer concentration in the effluent remained constant and was equal to the input tracer concentrations. This experimental design allowed the determination of solute tracer concentrations directly from the imaged bulk electrical conductivity measured with ERT, as shown by Koestel et al. (2008). We adjusted the temperature-corrected tap water background conductivity to 503 μS cm^{-1} for the LS column and to 590 μS cm^{-1} for the S columns using $CaCl_2$. The tracer conductivities were 2530 and 2630 μS cm^{-1}, respectively. The concentrations in the effluent were equal to the input concentrations after 36 and 64 d of tracer application in the LS and S soils, respectively.

Time-Lapse Electrical Resistivity Tomography

Forward Problem and Inversion Algorithm

We used a three-dimensional inversion of the ERT data to image changes in the soil bulk electrical conductivity, EC_b. A "skip one" dipole–dipole scheme was used as described in Slater and Sandberg (2000). Half of the measurements were run in a reciprocal mode to assess the data quality (LaBrecque et al., 1996; Koestel et al., 2008). Specifications of the measurement scheme can be found in Koestel et al. (2008). For all lysimeters, a finite element method was used to solve the forward problem, which was formulated as the Poisson equation:

$$\nabla\cdot(\sigma\nabla\phi)-\nabla\cdot j_s=0 \qquad [1]$$

where σ is the electrical conductivity, Φ is the electric potential, and j_s is the source current density. No-flow boundary conditions were applied on all boundaries.

Table 2. Average volumetric water content, θ, during the experiment measured with time domain reflectometry at five depths in the loamy sand lysimeter (LS), silty soil lysimeter (S1), and silty soil lysimeter (S2).

LS		S1		S2	
Depth	θ	Depth	θ	Depth	θ
cm		cm		cm	
−17.5	0.25	−22.5	0.43	−19.5	0.39
−42.5	0.19	−47.5	0.4	−44.5	0.38
−67.5	0.19	−72.5	0.4	−69.5	0.4
−92.5	0.19	−97.5	0.39	−94.5	0.4
−117.5	0.3	−122.5	0.4	−199.5	0.4

The inversion was performed using an error-weighted, smoothness-constrained, Occam-type algorithm. This means that the smoothest model distribution was searched to fit the data to a specified error level, ε_i. Given a set of N measurements of four-electrode resistance, R_i ($i = 1, 2, ..., N$), minimization of the objective function Ψ, given by

$$\Psi = \left\| \mathbf{W}_\varepsilon \left[\mathbf{d} - \mathbf{f}(\mathbf{m}) \right] \right\|_2^2 + \lambda \left\| \mathbf{W}_s (\mathbf{m} - \mathbf{m_0}) \right\|_2^2 \qquad [2]$$

produces an image of M voxel electrical resistivities, ρ_j ($j = 1, 2, ..., M$). Here, $\mathbf{d}$ is the data vector, given by

$$d_i = -\log(\rho_{a i}) \qquad i = 1, 2, ..., N \qquad [3]$$

where $\rho_{a i}$ is the ith apparent resistivity. The parameters of the inversion, $\mathbf{m}$, are given by

$$m_j = -\log(\rho_j) \qquad j = 1, 2, ..., M \qquad [4]$$

where $f(\mathbf{m})$ is the forward model for the model vector $\mathbf{m}$, m_0 is the starting or reference model, $\mathbf{W}_\varepsilon$ is an error weighting matrix (see Table 3 for the definition), $\mathbf{W}_s$ is a smoothness operator calculated from the discretized first or second derivative of $\mathbf{m}$, and λ is a regularization parameter that determines the amount of smoothing imposed on $\mathbf{m}$ during the inversion (see Table 3). For further details we refer to Kemna (2000) and Günther et al. (2006).

As the minimization of the objective function is done using the Tikhonov approach, both the minimization of Ψ and the adjustment of λ are intimately intertwined (Kemna, 2000). If the optimum value of λ is found using a univariate search, the minimization procedure finds the value of λ fitting the data to the desired target misfit. This implies that the smoothness of the final inversion result is affected by the error estimates ε_i. Therefore, a good estimation of the real data error is important.

Table 3. Overview of the inversion parameters and methodology for the two different codes used in this study.

Parameter	Gleyic Cambisol (loamy sand) Code A. Binley	Orthic Luvisol (silty S1 and S2) Code BERT T. Günther
Measurements		
Measurement scheme	Skip one dipole–dipole	
Measured combinations	46,260	27,077
Length time frame	8 h 23 min	5 h 50 min
Frequency	1 frame d^{-1}	2 frames d^{-1}
Vertical dipole length	25 cm	
Horizontal dipole length	22.8 cm	
Forward problem		
Numerical calculation of the electric field	finite element	finite element
Forward mesh	structured triangular prism mesh	unstructured tetrahedral mesh
Forward mesh resolution	edge length ~6 cm	variable
df of forward mesh	8472 nodes	33,365 nodes
df of primary mesh	–	125,420 nodes
More information	Binley et al. (1996)	Günther et al. (2006)
Inversion		
Meshes	dual grid approach	triple grid approach with singularity removal
Objective function minimization	Gauss–Newton minimization	Gauss–Newton minimization
Data functional		
Data vector	$d_i = -\log(\rho_{a i})$	$d_i = \log(\rho_{a i})$
Data weighting matrix	$\mathbf{W}_\varepsilon = \mathrm{diag}[1/\varepsilon_1, ..., 1/\varepsilon_N]$	$\mathbf{W}_\varepsilon = \mathrm{diag}[1/\log(1+\varepsilon_i)]$
Model functional		
Parameters of the inversion	$m_j = -\log(\rho_j)$	$m_j = \log(\rho_j)$
Reference model	none: $m_0 = [0...0]$	time lapse: $m_0 = m_{\mathrm{initial}}$
Smoothness operator	discretized second derivative	discretized first derivative
Regularization parameter	univariate line search (as in Labrecque et al., 1996)	constant λ
df of parameter mesh	2453 elements	20,434 elements

Electrical Resistivity Tomography Data Error Analysis

As suggested by Koestel et al. (2009), we assumed that the data error could be approximated using a Gaussian error model, which comprises an absolute resistance error component, a (Ω), and a relative resistance error component, b (dimensionless). These two components were then used in the inversion algorithm to calculate the error (ε_i) of each single data point d_i as follows:

$$\varepsilon_i = \frac{a}{R_i} + b \qquad [5]$$

We applied the approach proposed by Koestel et al. (2008) and used the normal-reciprocal error ($\varepsilon_{N/R}$) as a starting and reference point for the parameterization of the Gaussian error model. This approach considers the error model to be spatially and temporally constant in order to reduce the degrees of freedom in the error estimation.

Koestel et al. (2008) showed that the model for the normal-reciprocal error is spatially variable, not only because of varying solute concentrations but also because of varying water content. For the measurements of the LS soil, the mean of the error model parameter a was found to be 0.009 Ω (maximum 0.031 Ω), whereas the mean of parameter b was 0.5% (maximum 1.1%). For the S soil, the mean of a was 0.0041 Ω (maximum 0.0072 Ω), whereas the mean of b was 1.9% (maximum 3.3%). We discarded all data points that

had an $\varepsilon_{N/R}$ larger than five times the fitted error model in one or more of the time frames to maintain a similar sensitivity distribution throughout the experiment.

Time-Domain Reflectometry

Topp's equation (Topp, 1980) was used to relate the volumetric water content of the soil columns, θ, to the composite dielectric constant, ξ_c:

$$\theta = -5.3\times10^{-2} + \left(2.92\times10^{-2}\right)\xi_c - \left(5.5\times10^{-4}\right)\xi_c^2 + \left(4.3\times10^{-6}\right)\xi_c^3 \quad [6]$$

This calibration curve proved to be successful in soils that did not contain substantial amounts of bound water (Robinson et al., 2003).

In addition to water content, the EC_b was measured with TDR and served as a control measurement for the ERT data. The EC_b (μS cm^{-1}) was obtained from the TDR signal attenuation for measurement times much greater than the main detection of the reflected signal. We related the signal attenuation to the bulk electrical conductivity of the soil in the vicinity of the TDR rods using the relationship (Heimovaara, 1995; Mallants et al., 1996)

$$EC_b = \frac{K_p}{R_{TDR} - R_{Cable}} \quad [7]$$

where K_p is the cell constant of the TDR probe, R_{Cable} is the resistance associated with the cable tester, multiplexers, and connecters, and R_{TDR} is the ohmic resistance measured by the TDR. The value of R_{TDR} is derived from ρ_∞, the reflection coefficient at very long times, and is defined as

$$R_{TDR} = Z_C\frac{(1+\rho_\infty)}{(1-\rho_\infty)} \quad [8]$$

where Z_C is the impedance of the TDR device, multiplexer, and cable. Both K_p and R_{Cable} were determined for each probe individually using calibration measurements. The precision of the TDR probes was investigated during a period of 10 consecutive days under hydraulic and chemical steady-state conditions. The CV for the EC_b measurements during this period was always ≤2%. We also inferred the TDR accuracy by fitting the measured EC to Eq. [7] for 10 different calibration solutions and calculating the residual. Given the EC_b values that we measured during the experiment (25–300 μS cm^{-1} for the LS lysimeter and 140–800 μS cm^{-1} for the S lysimeters), we can infer a TDR accuracy of 4% or better for EC measurements in the LS soil and of 7% or better for the S soil.

Monitoring Solute Concentration

The EC_b was assumed to be linearly related to the solute electrical conductivity (EC_w). The calibration parameters of this relationship depend on the volumetric water content and soil properties like porosity, pore connectivity, and electrical conductance of the electrical double layer that surrounds the soil particles. These variables and properties vary with the location within the soil monolith. Based on EC_b measurements at the start (t_0) and the end (t_{end}) of the experiment, the parameters of the relationship between EC_b and EC_w were derived for every pixel in the soil column as in Koestel et al. (2008) using the following:

$$EC_w(t) = \frac{EC_b(t) - EC_b(t_0)}{EC_b(t_{end}) - EC_b(t_0)} \times \left[EC_w(t_{end}) - EC_w(t_0)\right] + EC_w(t_0) \quad [9]$$

Note that the water content was constant with time within the soil column during the experiment.

Inferring Transport Parameters

The CDE is the most widely used model to interpret and characterize tracer experiments (Vanderborght and Vereecken, 2007). The apparent velocity, v, represents the transport velocity of the solute front in the vertical direction, whereas the apparent dispersivity, λ, characterizes the variance of the solute arrival time at a certain point in a given realization of the velocity field (Vanderborght et al., 2006). To characterize the transport process at different vertical and horizontal scales, the CDE was fitted to breakthrough curves (BTCs) of the $CaCl_2$ tracer or changes in the electrical conductivity that were observed at different depths within the soil monolith and that were averaged across different horizontal scales:

$$\frac{\partial EC}{\partial t} = \lambda v\frac{\partial^2 EC}{\partial z^2} - v\frac{\partial EC}{\partial z} \quad [10]$$

where EC is the electrical conductivity, v (cm d^{-1}) and λ (cm) are the velocity and dispersivity, respectively, and z (cm) is the vertical coordinate.

A solution of the CDE for a first and third type top surface boundary condition was fitted to BTCs that were observed in the effluent of the column and BTCs that were observed within the column, respectively (van Genuchten and Parker, 1984).

In the case where the CDE was fitted to locally observed BTCs, the locally observed breakthrough was interpreted as the result of an equivalent one-dimensional convection–dispersion process (CDE) along a one-dimensional stream tube. This approach conceptualizes the soil as an ensemble of independent vertical stream tubes (stream tube model) that represent the complex three-dimensional flow field. The number of stream tubes used in the analysis depends on the resolution of the measurement method. For ERT measurements, the number of stream tubes at a certain depth depends on the number of voxels of the inversion mesh intersecting that depth. For the LS, this resulted in 640 stream tubes; for the finer mesh of the S1 and S2 lysimeters, it resulted in 1115.

The water distribution in the soil columns was not assumed to be homogeneous. In fact, we did not know the local water flux at any certain location in the lysimeter. As a consequence, smaller apparent velocities may also be due to local smaller water fluxes. For instance, a BTC that is observed in a region that is, to a large part, bypassed by the flow, and in which the flow rate is much smaller than the average flow rate, will have a smaller velocity than the average velocity.

Different Observation Scales

To investigate different manifestations of preferential flow, we observed tracer transport in the lysimeters at different scales. We distinguished three lateral observation scales and two vertical scales (see Table 4). In the lateral direction, the first observation scale corresponded to the scale of an individual voxel of the ERT mesh (subscript *vox*), i.e., approximately 7-cm length. The second lateral observation scale was related to the TDR measurement scale (subscript *tdr*), which corresponds to the size of the measurement volume of an individual TDR probe based on Ferré et al. (1998). This is a cylinder with a length equal to the length of the probes (~20 cm) and a radius of twice the distance between two rods of the probe. The third lateral observation scale investigated in this study was the column scale (subscript *col*) (116 cm). The column scale transport was represented by the concentrations or electrical conductivities in the effluent of the column and by horizontally averaged conductivities within the soil column, which were derived from the ERT measurements. It must be noted that preferential flow paths with a smaller dimension than the voxel scale may still be detected as a rapid increase in breakthrough that is followed by a long tailing of the breakthrough in that voxel.

In the vertical direction, two observation scales were distinguished that are related to the local and integral transport distance, respectively. The integral transport distance refers to the transport parameterization along a stream tube between the soil surface and a given depth. The integral velocity, v, is obtained directly from the CDE fit to the BTC of a voxel at a certain depth z_i. It is the integrated velocity along the trajectory of a solute particle from the soil surface to the observation depth. The local transport parameters refer to the transport process between two observation depths. We considered a local transport distance of 25 cm, which corresponds to the distance between the TDR probes in the soil columns. The local velocity, u, at depth z_i was then calculated from $v(z_{i+2})$ and $v(z_{i-2})$ as follows:

$$u_{z,i} = \frac{z_{i+2} - z_{i-2}}{\left[z_{i+2}/v\left(z_{i+2}\right)\right] - \left[z_{i-2}/v\left(z_{i-2}\right)\right]} \qquad [11]$$

where i denotes the ith horizontal voxel node layer starting from the soil surface to the bottom of the lysimeters. The LS mesh had 23 voxel node layers and S1 and S2 had 59.

Table 4. Overview of the different observation scales in the lysimeters and the corresponding measurement methods of electrical resistivity tomography (ERT), time domain reflectometry (TDR), and effluent measurements.

	Vertical scale	
Horizontal scale	Integral	Local
Voxel (~7 cm)	ERT	ERT
TDR (~20 cm)	ERT, TDR	ERT
Column (~116 cm)	ERT, TDR, effluent	ERT

Lateral Mixing

As stated above, one manifestation of preferential flow is the lack of mixing or solute mass exchange between regions with low and high advection velocities. This leads to a stronger increase of the solute spreading in the vertical direction than predicted by a convective–dispersive transport model. The nature of the mixing regime may be derived from the change in the apparent dispersivity with transport distance. A linear increase of dispersivity with transport distance indicates no mixing or a stochastic–convective process, whereas a constant dispersivity is a sign of perfect mixing or a convective–dispersive regime. In addition to mixing processes, vertical variations in soil properties (soil layering) may also lead to changes in dispersivity with depth. Other parameters that are more direct indicators of the mixing regime are the CVs of the local and integral velocities (Koestel et al., 2009). A decreasing CV(v) with travel distance indicates lateral mixing if, at the same time, the corresponding CV(u) remains constant. For a constant CV(u) with depth, a constant CV(v) indicates that no lateral mixing occurs (Javaux and Vanclooster, 2003). The CVs were calculated for the integral and local voxel-scale velocities, v and u, respectively, as follows:

$$\mathrm{CV}(v) = \frac{\sqrt{\mathrm{var}\left(v_{\mathrm{vox,ERT}}\right)}}{\overline{v}_{\mathrm{vox,ERT}}}$$

and [12]

$$\mathrm{CV}(u) = \frac{\sqrt{\mathrm{var}\left(u_{\mathrm{vox,ERT}}\right)}}{\overline{u}_{\mathrm{vox,ERT}}}$$

Convective–dispersive transport is connected with a decreasing CV (v) for increasing travel distance, whereas the CV(u) stays approximately constant. If CV(u) as well as CV(v) stays constant with depth, however, the mixing is incomplete and stochastic–convective transport can be assumed (Javaux and Vanclooster, 2003).

Spatiotemporal Behavior of Solute Leaching

Several studies on solute transport in soils were done using multicompartment samplers (Poletika and Jury, 1994; Quisenberry et al., 1994; Buchter et al., 1995; de Rooij and Stagnitti, 2000) because these samplers provide information about the distribution of the solute in both space and time. The temporal aspect of solute

leaching is characterized by the BTC, which describes the travel time of the solute at a given depth (Bloem, 2008). Stagnitti et al. (1999) and de Rooij and Stagnitti (2000) indicated that the spatial variability of solute movement can be illustrated and quantified using the spatial solute distribution curve. This curve yields the total amount of leached solute as a function of the fraction of the total sampling area, with the sampled compartments sorted from high to low leaching rates. By plotting the BTCs of the individual compartments next to one another in order of decreasing total leaching, they introduced the *leaching surface*. The shape of this surface highlights the key features of the leaching process and facilitates the analysis of the combined variation of solute fluxes in space and time.

Leaching surfaces have been derived from local solute flux measurements after a Dirac pulse solute application. In our experiments, a step input was used and local resident solute concentrations were derived. As illustrated by Bloem et al. (2008), leaching surfaces that are derived from resident concentrations may differ substantially from solute flux leaching surfaces. We defined horizontal cross-sections or control planes in LS, S1, and S2 at the 108-, 106-, and 107-cm depths, respectively, and derived the BTCs for the voxels in these planes to derive the corresponding leaching surfaces. These voxel planes where chosen because they represent practically the same vertical tracer traveling distance for all three columns and they lie in the bottom part of the lysimeters. The step pulse BTCs were translated to BTCs resulting from a Dirac pulse using the fitted CDE parameters and the solution of the CDE for a Dirac tracer application and a first type boundary condition. The predicted concentrations were normalized by the zeroth moment of the BTC, and the normalized BTC represents a travel time distribution. Subsequently, the normalized solute flux, J_s (cm d^{-2}), was calculated by multiplying the normalized BTCs by the local velocity, u, and the volumetric water content, θ. Since the volumetric water content was not observed for each individual pixel, the average water content derived from the TDR measurements was used. The pixels in the control plane where then ranked in order of descending amount of cumulative leaching. Subsequently, we plotted the leaching surface, Surf(x,t) (cm^{-2} d^{-1}), as in de Rooij and Stagnitti (2002), whereby the horizontal x axis represents the cumulated area of the sorted pixels, the horizontal t axis represents the time, and the vertical axis the scaled flux, Surf(x,t). The scaled solute flux is defined as

$$\mathrm{Surf}(x,t) = J_s(x,t)\left[\int_{t_0}^{\infty}\int_{0}^{A} J_s(x,t)\,\mathrm{d}x\mathrm{d}t\right]^{-1} \qquad [13]$$

where t_0 is the application time and A is the area of the reference plane. A cross-section of Surf parallel to the x axis and at a certain point in time t^* gives the spatial solute distribution curve (SSDC):

$$\mathrm{SSDC}(x)\big|_{t^*} = \mathrm{Surf}(x,t^*) \qquad x\in[0,A] \qquad [14]$$

The scaled total amount leached (STAL) at the end of the experiment ($t^* = \infty$) for each pixel was calculated as follows

$$\mathrm{STAL}(x)\big|_{t^*} = \int_{t_0}^{t^*} \mathrm{Surf}(x,t)\,\mathrm{d}t \qquad x\in[0,A] \qquad [15]$$

We then calculated the cumulative spatial solute distribution curve, which represents the maximum fraction of the applied solute mass that leaches through a certain area within the reference plane (FTL):

$$\mathrm{FTL}(x) = \int_{0}^{x}\int_{t_0}^{\infty} \mathrm{Surf}(\chi,t)\,\mathrm{d}t\mathrm{d}\chi \qquad x\in[0,A] \qquad [16]$$

As in Stagnitti et al. (1999), we fitted the cumulative density of the standard β function to the curve resulting from FTL(x) and calculated the scaled heterogeneity index (HI) as

$$\mathrm{HI}(\alpha,\zeta) = \sqrt{\frac{3\zeta}{\alpha(\alpha+\zeta+1)}} \qquad [17]$$

where α and ζ are free parameters of the standard β function defined by Bronshstein and Semendyayev (1979).

Results

Three-Dimensional Distribution of the Pore Water Electrical Conductivity

Figure 4 shows the three-dimensional distribution of EC_w at three different stages of the experiment, when similar amounts of pore volumes were leached through the different soils. Although the tracer transport is not totally homogeneous in the LS (top line in Fig. 4), the tracer front does not have clear fingering or preferential flow patterns and we can still speak of rather homogeneous solute transport for this soil under the given boundary conditions. On the contrary, the tracer front in S1 is much more heterogeneous (bottom line of Fig. 4). In the first time step shown in the image, a preferential flow path or tongue can be seen in the bottom left area of the lysimeter. Figure 5 gives a more detailed representation. This tongue appeared at the very beginning of the experiment in the ERT time series and remained visible until about 1.5 mo after the start of the experiment. After that, the whole pore volume was slowly replaced by the applied tracer concentration. In the second lysimeter (S2), which was taken from the silty soil but which is not shown in Fig. 4, such distinct preferential flow paths were not observed, but similarly to the transport in S1, the initial pore water was gradually replaced by the infiltrating tracer solution. This is in contrast with the LS, in which the invading tracer front rapidly replaced the initial pore water.

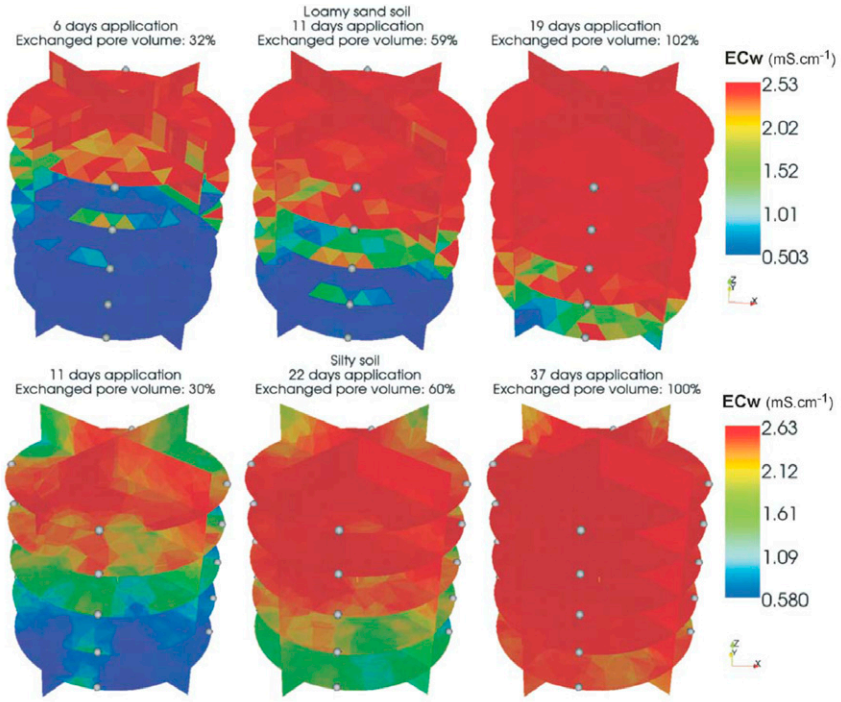

Fig. 4. Three-dimensional solute electrical conductivity (EC_w) for both lysimeter experiments: the loamy sand soil at t = 6, 11, and 19 d (top) and the silty soil S1 at t = 11, 22, and 37 d (bottom). The gray spheres represent time domain reflectometry probe locations in the lysimeters.

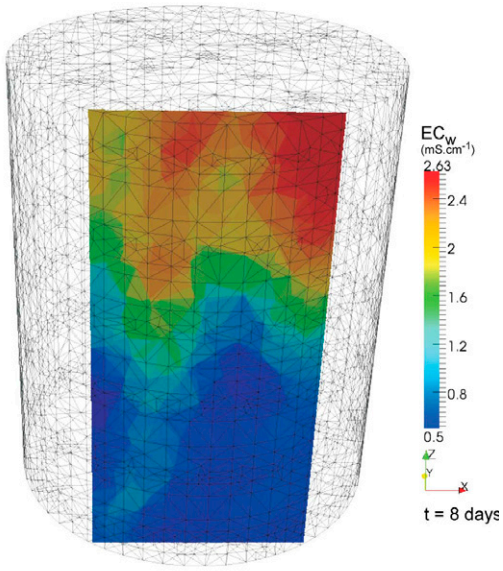

Fig. 5. Detail of a preferential flow tongue in terms of three-dimensional solute electrical conductivity (EC_w) after 8 d of tracer irrigation in Lysimeter S1.

Breakthrough Curves at Different Scales as Indicators of Heterogeneity and Preferential Flow Processes

Figure 6 shows the local (Fig. 6a) and column scale (Fig.6b) BTCs that were measured in the LS and S lysimeters. The BTCs are normalized by the total pore volume of the column. This is a way to normalize time for experiments in two different soils and, thus, it allows us to compare the shape of the BTCs. In the S soils, the local BTCs at one depth differ considerably in terms of arrival time, suggesting heterogeneous transport in the lysimeter. The TDR probe of the second transect that shows an early breakthrough is located close to the preferential flow path in the lysimeter (see Fig. 4 and 5). In general, there is a good agreement between ERT and TDR. The ERT-derived BTCs in the voxels located in the TDR sampling volume reproduce the tracer front arrival time measured by the TDR probes quite well; however, ERT seems to overestimate the spreading of the BTC. This effect stems from the smoothness-constrained inversion of the resistivity data (Kemna et al., 2002; Vanderborght et al., 2005). This overestimation of the spreading has an effect on the estimated dispersivities from the locally observed BTC in an ERT voxel, as will be shown below.

The BTCs that were measured in the effluent of the lysimeters correspond well with the column-scale averaged BTCs that were derived from ERT

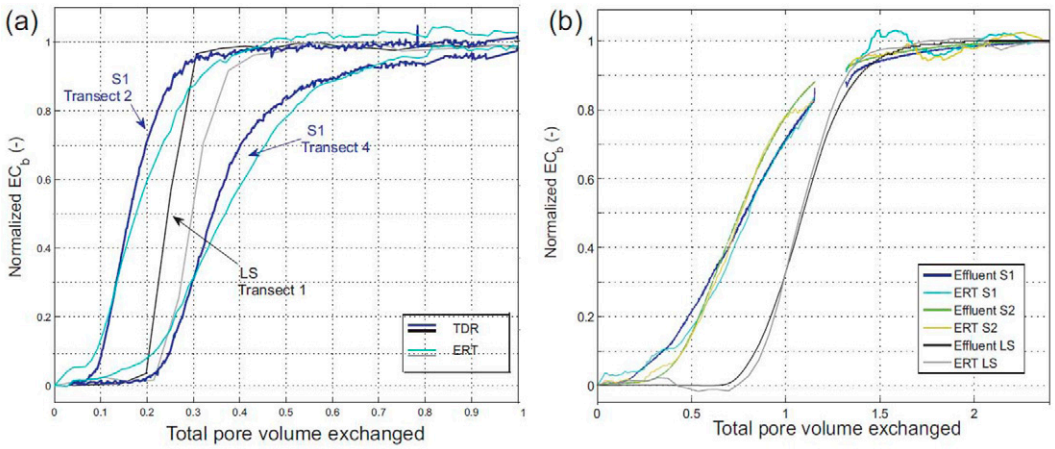

Fig. 6. Normalized breakthrough curves of (a) electrical resistivity tomography (ERT) and time domain reflectometry (TDR) for the steady-state tracer experiment in both soils at a depth of 47.5 cm (gray = loamy sand [LS] soil, blue = silt soil S1), and (b) column-scale averaged ERT and effluent conductivity measurements for the sand and silty soils (gray = LS, blue = S1, green = S2); EC_b is the bulk soil electrical conductivity.

measurements. The mean arrival time of the solute at the outlet is earlier in the S soil than in the LS soil if time is expressed in total pore volumes that are already exchanged. The column-scale BTCs also show a larger spreading in the S soil than in the LS soil, which again indicates a more heterogeneous transport in the S soil. It should also be noted that the preferential flow path that is observed in S1 corresponds to a more rapid increase of the tracer concentration in the effluent in S1 than in S2. This rapid increase in tracer concentration is not extremely evident, however, and from the shape of the BTC in the effluent of S1 it is hard to infer the presence of a preferential flow path in this lysimeter.

Characterization and Quantification of Heterogeneous Transport

Convection–Dispersion Parameters

Figure 7 shows the CDE parameters fitted to the TDR-scale BTCs measured with ERT and TDR. The apparent integral velocities, v, of the ERT and TDR measurements agree well, apart from two outliers for the S soils. The R^2 values are 0.975 for the LS and 0.593 for the ensemble of S1 and S2. The apparent dispersivities (λ) from both measurement methods also agree, but there are some deviations. For the S soils, the R^2 is rather low, at 0.308, whereas the LS has an R^2 of 0.774. The deviations are probably due to the effect of the smoothness constraints on the ERT BTCs. Some measurements were characterized by very high dispersivities. This was caused by BTCs obtained along the preferential flow path, which can have a bimodal breakthrough or a quick increase of solute concentration followed by an extremely long tailing. In these cases, the fitted CDE parameters do not represent the real breakthrough well.

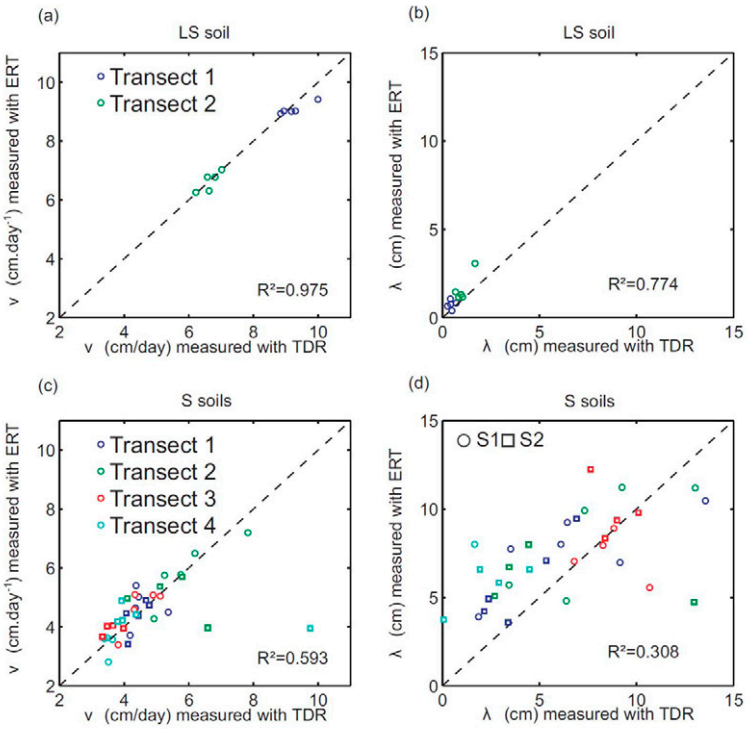

Fig. 7. Convective–dispersive equation parameters v and λ fitted to breakthrough curves (BTCs) of electrical resistivity tomography (ERT) and time domain reflectometry (TDR): (a) apparent velocity for the BTCs of the loamy sand (LS) soil, (b) apparent dispersivity for the BTCs of the LS, (c) apparent velocity for the BTCs of the silty (S) soils (S1, circle; S2, square), (d) apparent dispersivity for the BTCs of the S soils.

The apparent CDE parameters of the column-averaged data and effluent tracer breakthrough are plotted in Fig. 8 together with the average of the local-scale apparent CDE parameters. In general, there is a good agreement between parameters derived from ERT, TDR, and effluent measurements, except for the apparent dispersivities at some depths for the S monoliths. This can be explained by the fact that the column-scale dispersivity (λ_{col}) accounts for not only local-scale dispersion processes. It also contains the effect of the variation in stream tube velocity on the column-scale averaged breakthrough. This effect may be missing in the TDR-derived BTCs, as the number of TDR probes may have been too small to obtain a representative sample of the stream tube velocities.

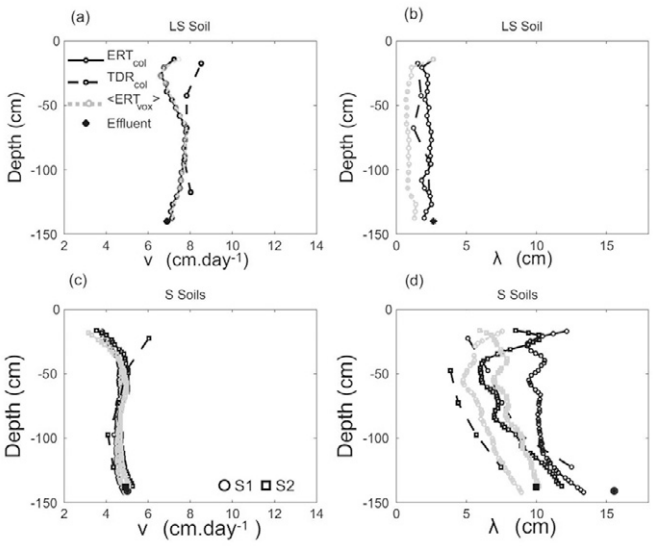

Fig. 8. Convective–dispersive equation (CDE) parameters apparent velocity v and apparent dispersivity λ fitted to the column-scale breakthrough curves (BTCs) from electrical resistivity tomography (ERT), time domain reflectometry (TDR), and effluent conductivity measurements and the average of the CDE parameters for the voxel-scale BTCs: (a) apparent velocity for the BTCs of the loamy sand (LS) soil, (b) apparent dispersivity for the BTCs of the LS, (c) apparent velocity for the BTCs of the silty (S) soils, and (d) apparent dispersivity for the BTCs of the S soils (S1, circle; S2, square).

As can be expected, the velocities at voxel, TDR, and column scales in the finer textured soils (S) were smaller than in the soil with the coarse texture (LS). The v_{tdr} and v_{vox} fitted to TDR and ERT BTCs varied mainly between 6 and 9 cm d^{-1} for the LS and between 3 and 5 cm d^{-1} for the S soil. The volumetric water content in the S soils was twice the water content in the LS soil (see

Table 2) and the saturated hydraulic conductivity of the LS soil was higher than those of the S soils (see Table 1). This can explain the fact that the transport was slower in the S soils. The voxel- and TDR-scale dispersivities (λ_{vox} and λ_{tdr}) in the LS soil lie between 1 and 2 cm, whereas those of the S are mainly between 3 and 10 cm. The S soils clearly had a larger dispersivity than the LS soil. The differences between the two soils are also visible at the column scale (see Fig. 8). In both soils, the column-scale dispersivity was larger than the voxel-scale dispersivity. This indicates that variations in the advection velocity that existed at a scale larger than the scale of an ERT voxel had an influence on the λ_{col} or solute spreading that was apparent at this scale. In S2, however, the λ_{vox} determined λ_{col} to a large extent because the difference between the average voxel-scale dispersivity, $<\lambda_{vox}>$, and λ_{col} is not large. This indicates that in S2, small-scale dispersion processes, which cannot be resolved by ERT, played an important role. In this case, the variation of the local velocity should not have an important impact on the solute spreading. The local velocity variance, however, is almost identical for both S1 and S2. This implies that the correlation scale of the local velocity must be larger in S1 than in S2. This is in line with the larger CV of the integral velocity in S1 than in S2. The different behavior of the column-scale dispersivity compared with the average of the voxel-scale dispersivity in S1 and S2 may thus be related to the vertical correlation of the advection velocities in the preferential flow path that was observed in S1.

An indicator for the identification of transport processes is the behavior of λ_{col} with depth. A linear increase in λ_{col} with travel distance indicates that lateral mixing is not complete. The solute transport process can then be described as stochastic–convective. In contrast, a constant λ_{col} indicates that solute spreading can be described as a diffusive or Fickian process (Roth and Hammel, 1996; Vanderborght et al., 2001). For the LS soil, there was no linear increase with depth (see Fig. 8). Thus, the transport can be called convective–dispersive. But S1 and S2 do have an increase in λ_{col} with depth, except for the top 25 cm. As Koestel et al. (2009) pointed out, the apparent dispersivity can only be used as an indicator of a mixing regime under the assumption that the local velocity variability remains constant and does not change with depth. For the LS soil, this is the case, but for both S1 and S2 it should be noted that there were important changes in variability of the local velocities between the soil layers (see Fig. 9). Therefore, it is not possible to draw an unambiguous conclusion about the transport behavior in the silt lysimeters.

The change in the CDE parameters with depth is another indicator to characterize solute transport processes. The CVs of velocity (integral and local) for both soils are plotted in Fig. 9. It can be seen that the CV of the integral apparent velocities [CV(v)] decreases with depth for all three lysimeters. Meanwhile, the CV of the local velocities [CV(u)] stays more or less constant for LS. As already pointed out by Koestel et al. (2009), this is an indication that the LS soil has a Fickian solute mixing regime. For S1 and S2, the effect

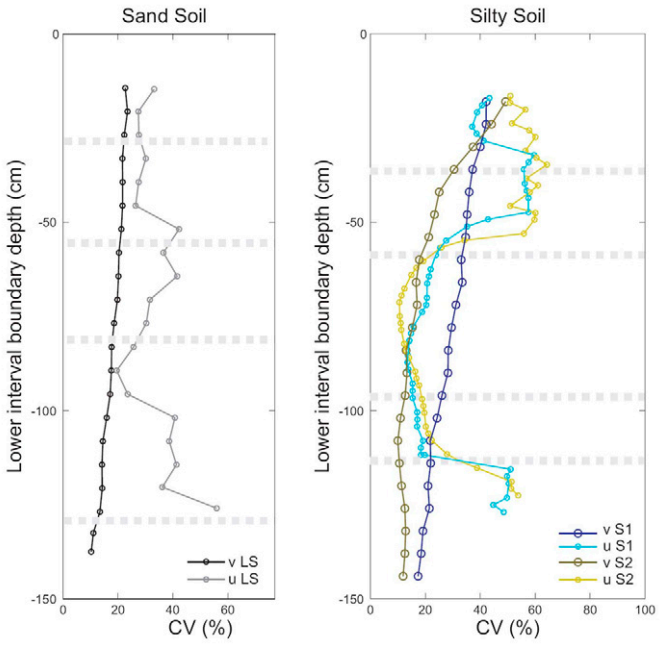

Fig. 9. Coefficients of variation of the voxel-scale integral, v, and local, u, velocities for the loamy sand (LS) soil (left) and silty soils (S1 and S2) (right). Horizon boundaries are indicated with dashed lines.

of soil layering on the CV(u) profile is clearly visible, which is not the case for LS. The plow horizon in this agricultural soil is rather deep and the depth of the boundary of the horizon varies between 30 and 44 cm according to several studies in the test field from which the lysimeters were taken (Pütz, 1993; Schmidt-Eisenlohr, 2001; Reinken, 2004; Burkhardt et al., 2005). The plow horizon seems to have had an impact on u in S1 and S2. In the second horizon, the CV(u) stays high for both S lysimeters and decreases abruptly thereafter. The sudden variation in local transport velocities across horizon interfaces may be due to a bad connectivity or redistribution between flow paths across the interfaces. In the neighborhood of the compacted plow pan, which is occasionally perforated with earthworm holes and roots (Burkhardt et al., 2005), the main transport direction may become more lateral than vertical. This indicates that our method to calculate the local velocity is not appropriate in this case. In between the abrupt changes, the CV(u) is constant with depth for S1 and S2. Until now, the effect of soil layers on the transport process has not been identified as clearly as we can see it in this study. Seuntjens et al. (2001) already showed, by measuring and analyzing BTCs with several TDR probes in different layers, that solute transport in a Spodosol is affected by the soil morphology. Electrical resistivity tomography, however, has allowed us to analyze the transport process in much more detail throughout the whole lysimeter volume and has made it possible to show the effect of soil morphology very clearly.

If we now compare Fig. 8 and 9, we can see that the decrease in the dispersivity in the S1 beneath a depth of approximately 20 cm corresponds to a decrease in the local velocity variance. In the deepest soil layer, the variance of the local velocity increases again

drastically and this is accompanied by a stronger increase with depth of the dispersivity in this layer. This is again a proof that the column-scale dispersivity in S1 depends on the variation in the local-scale velocities.

Leaching Surfaces

Figure 10 shows the local velocity-based leaching surfaces for both soils. The leaching surfaces are clearly different for the two soil types, which illustrates the different transport in the two soils. The S1 and S2 soils have a rather smooth leaching surface, with a very small portion showing a high peak. This high peak is most pronounced in S1, the lysimeter where a preferential flow path was detected with ERT. The leaching surface of the LS soil seems more irregular, which indicates that the local solute flux is not correlated with the tracer arrival at a certain location and that the spreading of the local BTCs does not override the variation in arrival time. Since the apparent dispersivities of the local BTCs are smaller and the apparent velocities are larger in the LS than in the S soil, the peaks in the leaching surface are larger in the LS than in the S1 and S2. Subsequently, we plotted the scaled total amount leached (STAL) for each area of the control plane and the fraction of the total leaching (FTL) in Fig. 11. The smaller the curvature (i.e., wider curve) of the FTL curve, the more evenly distributed is the leaching process. The curves of LS, S1, and S2 are similar, but some differences can be seen. The Kolmogorov–Smirnov test indicates that there is a significant difference between the LS and the S curves at a significance level of 13%.

The biggest difference between the LS and the S soils can be seen between STAL(x = 0.2) and STAL(x = 0.9). Except for a limited number of areas with very high and very low leaching, the total amount leached through the areas is similar in the LS soil, which follows from the nearly horizontal course of the STAL curve between x = 0.2 and x = 0.9. This is not the case for both S soils. The S1, the lysimeter with preferential flow behavior, has the highest STAL of all three lysimeters in the highest ranked areas. This indicates that only a small number of voxels is responsible for the spotted preferential flow path. The heterogeneity index (HI) of the LS soil is 1.14, whereas HI(S1) = 1.20 and HI(S2) = 1.18. As Stagnitti et al. (1999) showed, a uniform distribution of the solute transport throughout the control plane will result in a HI = 1. A nonuniform distribution is indicated when HI > 1 and the magnitude of the HI > 1 indicates the magnitude of the nonuniformity. The fact that HI is higher for the S soils than for the LS soil is also the result we would expect after observing the ERT data for the lysimeters; however, the difference between the HIs is rather small. De Rooij and Stagnitti (2000) reported a HI of 1.32 for a soil column from a sandy, mesic Typic Psammaquent. Steenhuis et al. (1990) indicated values between 1.31 and 1.56 for soil cores from a dark basaltic soil with a high organic content.

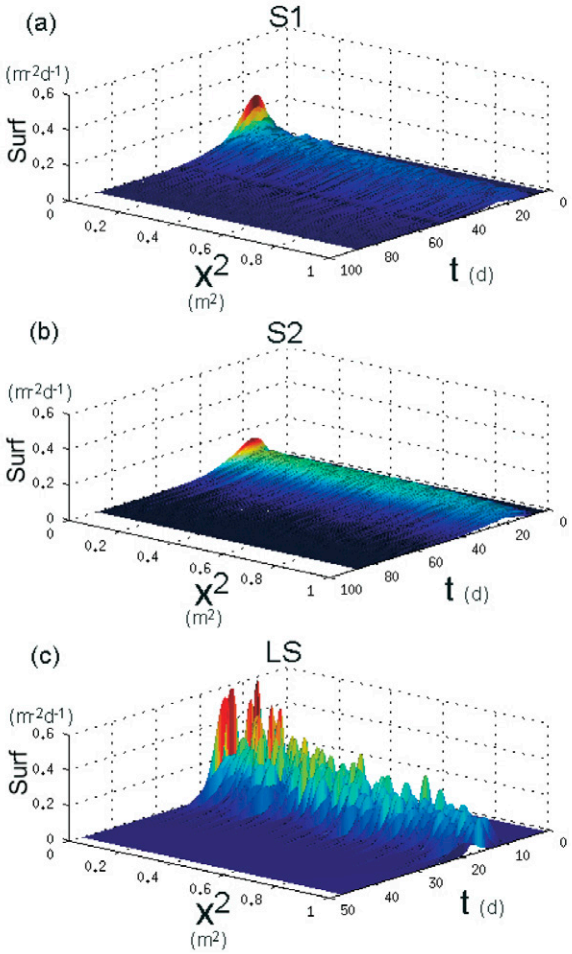

Fig. 10. Apparent velocity-based leaching surfaces for (a) silty soil S1, (b) silty soil S2, and (c) loamy sand soil LS. The plots (a) and (b) were built of 1115 observations, whereas plot (c) had 630 observations.

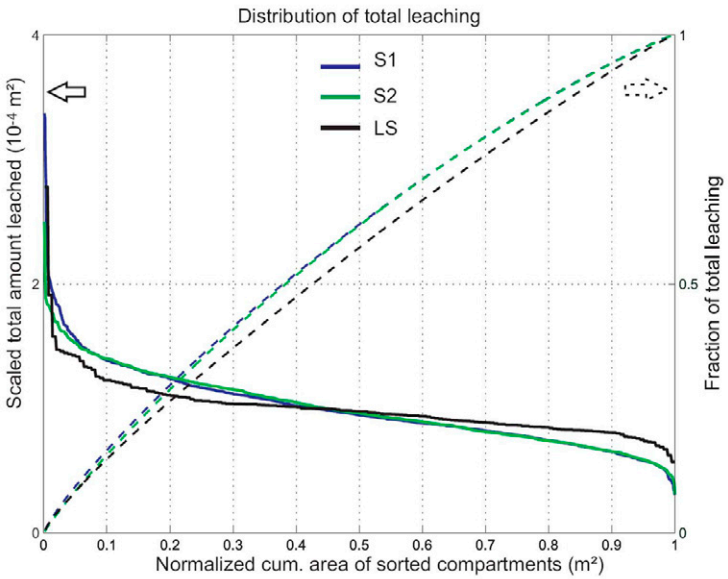

Fig. 11. Cumulative solute leaching for the control plane in all three lysimeters, loamy sand (LS) and two silty soils (S1 and S2).

Conclusions

In this study, we compared solute transport in two different unsaturated and undisturbed soils: a loamy sand (LS) and a silty soil (S). The solute transport in the two soils differed considerably in terms of heterogeneity, solute spreading, and the appearance of preferential transport. By using a noninvasive imaging technique, ERT, in combination with TDR measurements and concentration measurements in the effluent of the soil column, different aspects of the transport process and manifestations of preferential flow within two different soil types were investigated. We used voxel- and column-scale effective CDE parameters, leaching surfaces, and local velocities that were derived from the imaged tracer front movement to analyze the observed transport processes.

The presence of a constant apparent column-scale dispersivity with depth in the LS soil, combined with a decrease in the CV of the apparent integral velocity and a rather constant CV of the local velocity suggested a complete lateral solute mixing and therefore a convective–dispersive transport process at the lysimeter scale. The irregular leaching surface and the difference between the local- and column-scale dispersivities, however, pointed at the presence of a heterogeneous transport process and preferential flow within this soil leading to spatial variations of local solute concentration in a horizontal plane. This implies that a transport process that appears homogeneous at a larger scale may hide preferential transport at smaller scales.

Transport in the S1 and S2 lysimeters was considerably more heterogeneous than in the LS lysimeter, as indicated by the larger apparent column-scale dispersivity and the smaller lateral mixing. Analysis of the leaching process in the S1 and S2 lysimeters showed a distinct preferential flow path in S1 that was not observed in the LS lysimeter and that affected the column-scale averaged BTC; however, inference of the presence of such a preferential flow path from this BTC seems impossible. Despite the fact that its presence is hardly reflected in the effluent of the salt tracer, this preferential flow path may have large impacts on the transport and leaching of reactive tracers. Analysis of the leaching surfaces at selected reference planes was shown to be more suited to infer the presence of such preferential flow paths than the analysis of effluent data. A major part of the solute spreading that was observed in the effluent of the S soil was caused by small-scale dispersion processes, as indicated by the smooth leaching surfaces and the large voxel-scale dispersivities. Besides the large voxel-scale dispersion, there was still an important variability in advection velocity. Our analysis showed that the variability of local-scale velocities changed considerably across soil layer boundaries due to considerable differences in their transport properties. These properties are difficult to infer from a few local-scale measured BTCs. Using noninvasive techniques, BTCs can be derived on a grid of locations from which local velocities can be inferred. These velocity distributions were closely linked with soil layers in the S soil. Furthermore, they could be used to derive leaching surfaces in situ, which is important to identify the presence of preferential flow paths.

Acknowledgments

We would like to thank Dr. Thomas Pütz and Werner Mittelstaedt for the excavation of the lysimeters at both field sites, as well as Ansgar Weuthen, Normen Hermes, Ferdinand Engels, and Jürgen Höltkemeier for the technical design and support. We thank our colleague Michel Bechtold for fruitful discussions and help during the experiments. This project was financed by the Helmholtz virtual institute 'Inverse Modelling of Terrestrial Systems' INVEST.

References

Adams, E.E., and L.W. Gelhar. 1992. Field study of dispersion in a heterogeneous aquifer: 2. Spatial moments analysis. Water Resour. Res. 28:3293–3307.

al Hagrey, S.A., and J. Michaelson. 1999. Resistivity and percolation study of preferential flow in vadose zone at Bokhorst, Germany. Geophysics 64:746–753.

Aris, R. 1958. On the dispersion of linear kinematic waves. Proc. R. Soc. London Ser. A 245:268–277.

Binley, A., B. Shaw, and S.H. Poulter. 1996. Flow pathways in porous media: Electrical resistance tomography and dye staining image verification. Meas. Sci. Technol. 7:384–390.

Bloem, E. 2008. Variation in space and time of water flow and solute transport in heterogeneous soils and aquifers: A new multi-compartment percolation sampler and a new parameterization of the spatio-temporal solute distribution. Ph.D. diss. Wageningen Univ., Wageningen, the Netherlands.

Bloem, E., F.A.N. Hogervorst, and G.H. de Rooij. 2009. A field experiment with variable-suction multi-compartment samplers to measure the spatio-temporal distribution of solute leaching in an agricultural soil. J. Contam. Hydrol. 105:131–145.

Bloem, E., J. Vanderborght, and G.H. de Rooij. 2008. Leaching surfaces to characterize transport in a heterogeneous aquifer: Comparison between flux concentrations, resident concentrations, and flux concentrations estimated from temporal moment analysis. Water Resour. Res. 44:W10412, doi:10.1029/2007WR006425.

Bronshstein, I.N., and K.A. Semendyayev. 1979. Handbook of mathematics. Van Nostrand Reinhold, Frankfurt/Main, Germany.

Buchter, B., C. Hinz, M. Flury, and H. Flühler. 1995. Heterogeneous flow and solute transport in an unsaturated stony soil monolith. Soil Sci. Soc. Am. J. 59:14–21.

Burkhardt, M., R. Kasteel, S. Giesa, and H. Vereecken. 2005. Characterization of field tracer transport using high-resolution images. Vadose Zone J. 4:101–111.

Cirpka, O.A., R.L. Schwede, J. Luo, and M. Dentz. 2008. Concentration statistics for mixing-controlled reactive transport in random heterogeneous media. J. Contam. Hydrol. 98:61–74.

Clothier, B.E., S.R. Green, and M. Deurer. 2008. Preferential flow and transport in soil: Progress and prognosis. Eur. J. Soil Sci. 59:2–13.

de Rooij, G.H., O.A. Cirpka, F. Stagnitti, S.H. Vuurens, and J. Boll. 2006. Quantifying minimum monolith size and solute dilution from multi-compartment percolation sampler data. Vadose Zone J. 5:1086–1092.

de Rooij, G.H., and F. Stagnitti. 2000. Spatial variability of solute leaching: Experimental validation of a quantitative parameterization. Soil Sci. Soc. Am. J. 64:499–504.

de Rooij, G.H., and F. Stagnitti. 2002. Spatial and temporal distribution of solute leaching in heterogeneous soils: Analysis and application to multi-sampler lysimeter data. J. Contam. Hydrol. 54:329–346.

Desmedt, F., and P.J. Wierenga. 1984. Solute transfer through columns of glass beads. Water Resour. Res. 20:225–232.

Edwards, W.M., M.J. Shipitalo, L.B. Owens, and W.A. Dick. 1992. Rainfall intensity affects transport of water and chemicals through macropores in no-till soil. Soil Sci. Soc. Am. J. 56:52–58.

FAO. 1998. World reference base for soil resources. World Soil Resour. Rep. FAO, Rome.

Ferré, P.A., J.H. Knight, D.L. Rudolph, and R.G. Kachanoski. 1998. The sample areas of conventional and alternative time domain reflectometry probes. Water Resour. Res. 34:2971–2979.

Feyen, J., D. Jacques, A. Timmerman, and J. Vanderborght. 1998. Modelling water flow and solute transport in heterogeneous soils: A review of recent approaches. J. Agric. Eng. Res. 70:231–256.

Flury, M., H. Flühler, W.A. Jury, and J. Leuenberger. 1994. Susceptibility of soils to preferential flow of water: A field study. Water Resour. Res. 30:1945–1954.

Flury, M., and N.N. Wai. 2003. Dyes as tracers for vadose zone hydrology. Rev. Geophys. 41(1):1002, doi:10.1029/2001RG000109.

French, H.K., C. Hardbattle, A. Binley, P. Winship, and L. Jakobsen. 2002. Monitoring snowmelt induced unsaturated flow and transport using electrical resistivity tomography. J. Hydrol. 267:273–284.

Freyberg, D.L. 1986. A natural gradient experiment on solute transport in sand aquifer: 2. Spatial moments and the advection and dispersion of nonreactive tracers. Water Resour. Res. 22:2031–2046.

Gjettermann, B., K.L. Nielsen, C.T. Petersen, H.E. Jensen, and S. Hansen. 1997. Preferential flow in sandy loam soils as affected by irrigation intensity. Soil Technol. 11:139–152.

Günther, T., C. Rücker, and K. Spitzer. 2006. Three-dimensional modelling and inversion of DC resistivity data incorporating topography: II. Inversion. Geophys. J. Int. 166:506–517.

Heimovaara, T.J. 1993. Design of triple-wire time domain reflectometry probes in practice and theory. Soil Sci. Soc. Am. J. 57:1410–1417.

Heimovaara, T.J. 1995. Assessing temporal variations in soil water composition with time domain reflectometry. Soil Sci. Soc. Am. J. 59:689–698.

Herrmann, K.H., A. Pohlmeier, D. Gembris, and H. Vereecken. 2002. Three-dimensional imaging of pore water diffusion and motion in porous media by nuclear magnetic resonance imaging. J. Hydrol. 267:244–257.

Hoffman, F., D. Ronen, and Z. Pearl. 1996. Evaluation of flow characteristics of a sand column using magnetic resonance imaging. J. Contam. Hydrol. 22:95–107.

Javaux, M., R. Kasteel, J. Vanderborght, and M. Vanclooster. 2006. Interpretation of dye transport in a macroscopically heterogeneous, unsaturated subsoil with a one-dimensional model. Vadose Zone J. 5:529–538.

Javaux, M., and M. Vanclooster. 2003. Scale- and rate-dependent solute transport within an unsaturated sandy monolith. Soil Sci. Soc. Am. J. 67:1334–1343.

Jaynes, D.B., S.I. Ahmed, K.-J.S. Kung, and R.S. Kanwar. 2001. Temporal dynamics of preferential flow to a subsurface drain. Soil Sci. Soc. Am. J. 65:1368–1376.

Jury, W.A., and K. Roth. 1990. Transfer functions and solute movement through soil: Theory and applications. Birkhäuser Verlag, Basel, Switzerland.

Kasteel, R., H.J. Vogel, and K. Roth. 2002. Effect of non-linear adsorption on the transport behaviour of Brilliant Blue in a field soil. Eur. J. Soil Sci. 53:231–240.

Kemna, A. 2000. Tomographic inversion of complex resistivity: Theory and application. Der Andere Verlag, Osnabrück, Germany.

Kemna, A., J. Vanderborght, B. Kulessa, and H. Vereecken. 2002. Imaging and characterisation of subsurface solute transport using electrical resistivity tomography (ERT) and equivalent transport models. J. Hydrol. 267:125–146.

Kitanidis, P.K. 1994. The concept of the dilution index. Water Resour. Res. 30:2011–2026.

Koestel, J., A. Kemna, M. Javaux, A. Binley, and H. Vereecken. 2008. Quantitative imaging of solute transport in an unsaturated and undisturbed soil monolith with 3-D ERT and TDR. Water Resour. Res. 44:W12411, doi:10.1029/2007WR006755.

Koestel, J., J. Vanderborght, M. Javaux, A. Kemna, A. Binley, and H. Vereecken. 2009. Noninvasive 3-D transport characterization in a sandy soil using ERT: 2. Transport process inference. Vadose Zone J. 8:1–13.

Kreft, A., and A. Zuber. 1978. On the physical meaning of the dispersion equation and its solutions for different initial and boundary conditions. Chem. Eng. Sci. 33:1471–1480.

LaBrecque, D.J., M. Miletto, W. Daily, A. Ramirez, and E. Owen. 1996. The effects of noise on Occam's inversion of resistivity tomography data. Geophysics 61:538–548.

Looms, M.C., K.H. Jensen, A. Binley, and L. Nielsen. 2008. Monitoring unsaturated flow and transport using cross-borehole geophysical methods. Vadose Zone J. 7:227–237.

Mallants, D., M. Vanclooster, N. Toride, J. Vanderborght, M.Th. van Genuchten, and J. Feyen. 1996. Comparison of three methods to calibrate TDR for monitoring solute movement in undisturbed soil. Soil Sci. Soc. Am. J. 60:747–754.

Mooney, S.J., and C. Morris. 2008. A morphological approach to understanding preferential flow using image analysis with dye tracers and x-ray computed tomography. Catena 73:204–211.

Olsen, P.A., A. Binley, S. Henry-Poulter, and W. Tych. 1999. Characterizing solute transport in undisturbed soil cores using electrical and x-ray tomographic methods. Hydrol. Processes 13:211–221.

Oswald, S., W. Kinzelbach, A. Greiner, and G. Brix. 1997. Observation of flow and transport processes in artificial porous media via magnetic resonance imaging in three dimensions. Geoderma 80:417–429.

Poletika, N.N., and W.A. Jury. 1994. Effects of soil surface management on water flow distribution and solute dispersion. Soil Sci. Soc. Am. J. 58:999–1006.

Pütz, T. 1993. Lysimeterversuche zum Verlagerungsverhalten von Methabenzthiazuron und gelöstem organischen Kohlenstoff in einer Parabraunerde, Aufbau von zwei Klimameßstationen und Untersuchungen zur Validierung des Lysimetersystems. Berichte des Forschungszentrums Jülich, Jülich, Germany.

Quisenberry, V.L., R.E. Phillips, and J.M. Zeleznik. 1994. Spatial distribution of water and chloride macropore flow in a well-structured soil. Soil Sci. Soc. Am. J. 58:1294–1300.

Reinken, G. 2004. Bodenphysikalische Untersuchungen zur Prozeßanalyse der Wasserbewegung und des Stofftransportes in ungesättigten, strukturierten Böden unter besonderer Berücksichtigung der Mechanismen der präferentiellen Wirkstoffverlagerung. Ph.D. diss. Univ. of Köln, Köln, Germany.

Robinson, D.A., S.B. Jones, J.M. Wraith, D. Or, and S.P. Friedman. 2003. A review of advances in dielectric and electrical conductivity measurement in soils using time domain reflectometry. Vadose Zone J. 2:444–475.

Roth, K., and K. Hammel. 1996. Transport of conservative chemical through an unsaturated two-dimensional Miller-similar medium with steady state flow. Water Resour. Res. 32:1653–1663.

Salamon, P., D. Fernàndez-Garcia, and J.J. Gómez-Hernàndez. 2007. Modeling tracer transport at the MADE site: The importance of heterogeneity. Water Resour. Res. 43:W08404.

Sander, T., and H.H. Gerke. 2007. Preferential flow patterns in paddy fields using a dye tracer. Vadose Zone J. 6:105–115.

Schmidt-Eisenlohr, A. 2001. Räumliche und Zeitliche Variabilität von Bodenparametern und die Beschreibung des Wassertransports in einer Parabraunerde aus Schwemmlöß in der Jülicher Börde. Ph.D. diss. Rheinische Friedrich-Wilhelms Universität, Bonn, Germany.

Schoen, R., J.P. Gaudet, and T. Bariac. 1999. Preferential flow and solute transport in a large lysimeter, under controlled boundary conditions. J. Hydrol. 215:70–81.

Seuntjens, P., D. Mallants, N. Toride, C. Cornelis, and P. Geuzens. 2001. Grid lysimeter study of steady state chloride transport in two Spodosol types using TDR and wick samplers. J. Contam. Hydrol. 51:13–39.

Slater, L., A. Binley, R. Versteeg, G. Cassiani, R. Birken, and S. Sandberg. 2002. A 3D ERT study of solute transport in a large experimental tank. J. Appl. Geophys. 49:211–229.

Slater, L.D., and S.K. Sandberg. 2000. Resistivity and induced polarization monitoring of salt transport under natural hydraulic gradients. Geophysics 65:408–420.

Stagnitti, F., L. Li, G. Allinson, I. Phillips, D. Lockington, A. Zeiliguer, M. Allinson, J. Lloyd-Smith, and M. Xie. 1999. A mathematical model for estimating the extent of solute- and water-flux heterogeneity in multiple sample percolation experiments. J. Hydrol. 215:59–69.

Stagnitti, F., N. Villiers, J.-Y. Parlange, T.S. Steenhuis, G.H. de Rooij, L. Li, D.A. Barry, X. Xiong, and P. Li. 2003. Solute and contaminant transport in heterogeneous soils. Bull. Environ. Contam. Toxicol. 71:737–745.

Steenhuis, T.S., J.-Y. Parlange, and M.S. Andreini. 1990. A numerical model for preferential solute movement in structured soils. Geoderma 46:193–208.

Topp, G.C. 1980. Electromagnetic determination of soil water content: Measurements in coaxial transmission lines. Water Resour. Res. 16:574–582.

Vanderborght, J., D. Jacques, and J. Feyen. 2000a. Deriving transport parameters from transient flow leaching experiments by approximate steady-state flow convection–dispersion models. Soil Sci. Soc. Am. J. 64:1317–1327.

Vanderborght, J., R. Kasteel, and H. Vereecken. 2006. Stochastic continuum transport equations for field-scale solute transport: Overview of theoretical and experimental results. Vadose Zone J. 5:184–203.

Vanderborght, J., A. Kemna, H. Hardelauf, and H. Vereecken. 2005. Potential of electrical resistivity tomography to infer aquifer transport characteristics from tracer studies: A synthetic case study. Water Resour. Res. 41:W06013, doi:10.1029/2004WR003774.

Vanderborght, J., A. Timmerman, and J. Feyen. 2000b. Solute transport for steady-state and transient flow in soils with and without macropores. Soil Sci. Soc. Am. J. 64:1305–1317.

Vanderborght, J., M. Vanclooster, A. Timmerman, P. Seuntjens, D. Mallants, D.J. Kim, D. Jacques, L. Hubrechts, C. Gonzalez, J. Feyen, J. Diels, and J. Deckers. 2001. Overview of inert tracer experiments in key Belgian soil types: Relation between transport and soil morphological and hydraulic properties. Water Resour. Res. 37:2873–2888.

Vanderborght, J., and H. Vereecken. 2007. Review of dispersivities for transport modeling in soils. Vadose Zone J. 6:29–52.

van Genuchten, M.Th., and J.C. Parker. 1984. Boundary-conditions for displacement experiments through short laboratory soil columns. Soil Sci. Soc. Am. J. 48:703–708.

Weihermueller, L. 2005. Comparison of different soil water extraction systems for the prognoses of solute transport at the field scale using numerical simulations, field and lysimeter experiments. Diss. Rheinische Friedrich-Wilhelms Universität, Bonn, Germany.